Modal approach to quantum temporal imaging

G. Patera,[1,*] D. B. Horoshko,[1] M. Allgaier,[2] M. I. Kolobov,[1] and C. Silberhorn[3]
[1]*Université Lille, CNRS, UMR 8523 - PhLAM - Physique des Lasers Atomes et Molécules, F-59000 Lille, France*
[2]*Department of Physics and Oregon Center for Optical, Molecular, and Quantum Science, University of Oregon, Eugene, Oregon 97403, USA*
[3]*Integrated Quantum Optics Group, Applied Physics, University of Paderborn, 33098 Paderborn, Germany*

(Received 8 September 2023; accepted 25 September 2023; published 18 October 2023)

We consider the problem of quantum temporal imaging in the case where the time lens is implemented by a sum frequency generation nonlinear process, in particular when the device is operated in high conversion efficiency regimes. In the general case where the time lens also presents a finite aperture and a nonperfect phase matching, the relevant figures of merit, as for example the temporal resolution, do not have an explicit expression. As a consequence, the performances of the imaging scheme are difficult to assess. We show that this problem can be solved for conversion efficiencies up to 80% in terms of the eigenmodes of the imaging scheme, approximated by chirped Gauss-Hermite functions, and we show how its relevant figures of merit can be extracted from the modal description of the imaging scheme. As a consequence, we obtain criteria allowing one to design imaging schemes with high efficiencies.

DOI: 10.1103/PhysRevA.108.043716

I. INTRODUCTION

Optical spectrotemporal degrees of freedom of single photons provide a reliable platform for quantum information encoding [1,2]. Quantum applications enabled by this type of encoding include linear optics quantum computation [3,4], boson sampling [5,6], quantum communications [7,8], and quantum sensing [9,10]. Noiseless manipulation of a single-photon waveform plays an important role in the processing of quantum information and communication networks [11]. In order to cope with the great heterogeneity of technologies that are used in a quantum network [12], it is important to optimize mode matching between the nodes: to match the carrier frequency and to match the temporal scale. For this purpose, a plethora of strategies has been proposed such as translation of the carrier frequency [13–16], bandwidth compression or stretching at the same carrier frequency [17–19], simultaneous carrier frequency translation and bandwidth manipulation [20,21], and mode-selective operations such as waveform conversion [22], quantum pulse gating [23–28], and shaping [29,30].

Another approach to the manipulation of optical pulses is based on the formal space-time analogy between the propagation of a diffracting beam and that of a short pulse in dispersive media [31]. For classical beams, this led to the formulation of temporal imaging [32–36] and the demonstration of ultrafast waveform magnification and reversal [37,38], temporal compression [39], spectral magnification [40], spectral phase conjugation [41], or ultrafast waveform detection [42,43]. On the other side, quantum temporal imaging (QTI) aims at the manipulation of the time-frequency degrees of freedom of a quantum state without destroying it. This has been considered for single photons [17,18,44–47] and for squeezed light [48–52].

The key element of a temporal imaging system is the time lens, a device that imprints a quadratic temporal phase modulation on an input pulse, like a thin lens induces a quadratic phase modulation on a spatially extended input wave front. Optical time lenses are presently based on electro-optical phase modulation [17,19,32], sum-frequency generation (SFG) [37,38], or four-wave mixing (FWM) [39–42], and provide a temporal magnification above 100 times. Time lenses based on nonlinear processes, as discussed in [44,48–50], need to be operated in high conversion efficiency regimes in order to process an input quantum state without destroying its quantum properties. This case has been considered in the limit of infinite aperture and perfect phase matching [44,45,48,49], and in the limit of finite aperture but still perfect phase matching [51,52]. Here we consider the most general case of QTI with finite aperture and in the presence of nonperfect phase matching, developing the idea expressed in Ref. [53]. This case has been considered in [35], but only in the low conversion efficiency limit, a regime suitable for classical protocols only. On the contrary, in the high conversion efficiency regime, this problem does not admit a closed-form solution, and thus an explicit expression for the impulse response function (IRF) is not possible. The IRF represents the response of the system to a point object and plays an important role for extracting the relevant figures of merit—temporal resolution, temporal and spectral fields of view, etc.—and for assessing the system performances. Having a reliable estimation of these figures of merits is particularly important because they can be significantly different from the regime of low conversion efficiency usually considered in classical temporal imaging.

In this work, we show that for an SFG-based time lens with a conversion efficiency up to 80%, the problem can be solved in terms of the singular values and vectors of the temporal imaging system and its relevant figures of merit can be extracted from the modal description even if the IRF does not have an explicit expression. Our approach also allows

*Corresponding author: giuseppe.patera@univ-lille.fr

us to make clear the multimode nature of QTI, a character that is important for processing an image without distortions, thus enabling the design of schemes with close to unit efficiencies. Modal field decompositions from plane waves to resonator modes represent a versatile tool in optics [54]. The modal description of a spatial imaging system has been known for several decades for classical [55] and quantum [56] imaging and was used for the demonstration of optical super-resolution [57]. A direct transfer of this description into the temporal domain is, however, impossible because it is based on prolate spheroidal modes creating an eigenbasis of a diffraction-limited $4f$ system with circular or rectangular apertures. In contrast, the temporal aperture of a parametric time lens is determined by the temporal shape of the pump pulse, typically Gaussian, which results, as we show, in an eigenbasis of chirped Gauss-Hermite functions of frequency.

The basis of temporal Gauss-Hermite functions is being successfully used for the description of a device known as quantum pulse gate [23,25–27], also based on SFG with imperfect phase matching. However, this device is mode selective; its aim is to reach a unit conversion efficiency for one mode and zero for all other modes. In contrast, a temporal imaging system is intended to be mode nonselective and provide, in the ideal case, the unit conversion efficiency for all modes. Partial mode selectivity appears in a temporal imaging system because of finite aperture and imperfect phase matching, but is treated as an aberration.

The paper is structured as follows. In Sec. II, we review the formalism for the description of the two elements of a temporal imaging system, i.e., a dispersive medium and an SFG-based time lens, introducing a modal decomposition for the IRF of the latter. In Sec. III, we put these two elements together and develop a modal decomposition for the IRF of the entire temporal imaging system. The figures of merit are calculated from the characteristics of the modes in Sec. IV in different regimes of interest. The Conclusion in Sec. V summarizes the results. Appendix A reviews the decomposition of a complex double Gaussian into chirped Gauss-Hermite functions. Some properties of the latter, not found in the literature, are explored in Appendix B. The traditional approach to temporal imaging, based on the Fourier transform, is reviewed in Appendix C.

II. THE FORMALISM

In this paper, we consider the simplest imaging scheme that can be realized with a single time lens, as depicted in Fig. 1(a): it consists of a first dispersive medium followed by a time lens, then followed by a second dispersive medium. This scheme is the temporal equivalent of a thin lens that performs the imaging of a spatially extended object. In the following, we will refer to the first (second) medium as the *input* (*output*) dispersive medium. Without loss of generality, we will focus on a SFG-based time lens even if our approach also remains valid for FWM-based time lenses. The SFG process [see Fig. 1(b)] is mediated by a short chirped pump pulse of carrier frequency ω_p. Hence a pulse at signal frequency ω_s after a dispersive propagation through the input medium is up-converted in a nonlinear crystal to a new pulse at the idler frequency ω_i, such that $\omega_\mathrm{s}+\omega_\mathrm{p}=\omega_\mathrm{i}$. Finally, the

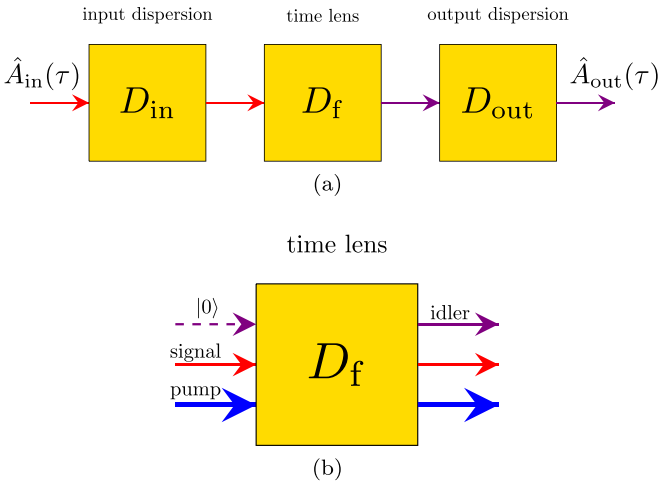

FIG. 1. (a) The imaging scheme: input dispersive line of total GDD, D_{in}, is followed by a time lens of focal GDD, D_{f}, and by an output dispersive line of total GDD, D_{out}. The input field $\hat{A}_{\mathrm{in}}(\tau)$ is imaged at the output on the field $\hat{A}_{\mathrm{out}}(\tau)$. (b) SFG-based time lens scheme: the signal field (red) is mixed together with a strong classical pump (blue) in order to produce the idler field (purple).

idler pulse is dispersed through the output medium. In the plane-wave and quasimonochromatic approximation, we write the positive-frequency electric field operator as

$$\hat{E}_m^{(+)}(t,z)=\mathcal{E}_m\, e^{i\left(k_m^0 z-\omega_m t\right)}\hat{A}_m\left(t-\beta_m^{(1)}z,z\right), \tag{1}$$

$$\hat{A}_m(\tau,z)=\int_{-\infty}^{+\infty}\frac{d\Omega}{2\pi}\, e^{-i\Omega\tau}\, e^{i\,\delta_m(\Omega)z}\hat{a}_m(\Omega,z), \tag{2}$$

where the index $m=\{s,i,p\}$ identifies the signal, idler, or pump waves, respectively, $\mathcal{E}_m$ is the single-photon amplitude, Ω is the detuning from the carrier frequency of the wave, $k_m^0=k_m(\omega_m)$ with $k_m(\omega)$ the wave vector of the corresponding wave at frequency ω, and $\delta_m(\Omega)=k(\omega_m+\Omega)-k_m^0-\beta_m^{(1)}\Omega$ with $\beta_m^{(1)}=(dk_m/d\omega)_{\omega_m}$ the inverse of group velocity of the corresponding wave. Equation (2) is written in the traveling-wave frame of reference (τ,z) propagating with the wave at pulse group velocity $1/\beta_m^{(1)}$ and τ has a meaning of *delayed time*. Note that when a wave passes through several media, the reference frame is delayed by the total group delay, summed up over all media [52].

A. Linear dispersion

In the quadratic dispersion approximation, the evolution of the $\hat{A}_m(\tau,z)$ fields through a dispersive medium of length L is given by

$$\hat{A}_m(\tau,z_0+L)=\int_{-\infty}^{+\infty}\frac{d\Omega}{2\pi}\, e^{-i\Omega\tau}\,\mathcal{G}(\Omega)\hat{a}_m(\Omega,z_0), \tag{3}$$

where

$$\mathcal{G}(\Omega)=e^{\frac{i}{2}D_m\Omega^2}, \tag{4}$$

$\beta_m^{(2)}=(d^2k_m/d\omega^2)_{\omega_m}$ is the group velocity dispersion (GVD), and $D_m=\beta_m^{(2)}L$ is the group delay dispersion (GDD) accumulated by the wave during its dispersive propagation through

the medium. Also, Eq. (3) can be rephrased as

$$\hat{A}_m(\tau, z_0 + L) = \int_{-\infty}^{+\infty} d\tau'\, e^{i\Omega\tau}\, G(\tau - \tau')\hat{A}_m(\tau', z_0), \quad (5)$$

with

$$G(\tau) = \frac{e^{-i\tau^2/2D_m}}{\sqrt{-i2\pi D_m}}. \quad (6)$$

Notice that Eqs. (3) and (5) induce a unitary transformation on the field operators, thus preserving their commutators.

B. Time lens

For a SFG-based time lens, the object pulse enters in the nonlinear medium through the input signal channel and is upconverted in the output idler mode [see Fig. 1(b)]. The input idler mode is in a vacuum state and the process is mediated by a strong undepleted pump. The evolution equations for the signal ($\hat{a}_\mathrm{s}$) and idler ($\hat{a}_\mathrm{i}$) fields through the nonlinear crystal, in the plane-wave and undepleted pump approximations, are given by the spatial Heisenberg equation [58],

$$\frac{\partial}{\partial z}\hat{a}_m(\Omega, z) = \frac{i}{\hbar}[\hat{a}_m(\Omega, z), \hat{H}(z)], \quad (7)$$

where the spatial Hamiltonian $\hat{H}(z)$ is given by the momentum transferred through the plane z [59],

$$\hat{H}(z) = \chi \int_{-\infty}^{+\infty} E_p^{(-)}(t, z)\hat{E}_s^{(-)}(t, z)\hat{E}_i^{(+)}(t, z)dt + \mathrm{H.c.}, \quad (8)$$

with χ the nonlinear coupling constant and $\hat{E}_m^{(-)}(t, z) = \hat{E}_m^{(+)\dagger}(t, z)$ the negative-frequency part of the field. Substituting Eqs. (1), (2), and (8) into Eq. (7), performing the integration over time, and using the canonical equal-space commutation relations [59,60],

$$[\hat{a}_m(\Omega, z), \hat{a}_m^\dagger(\Omega', z)] = 2\pi\delta(\Omega - \Omega'), \quad (9)$$

we obtain the spatial evolution equations,

$$\frac{\partial}{\partial z}\hat{a}_\mathrm{s}(\Omega, z) = g\int d\Omega' f^*(\Omega', \Omega, z)\hat{a}_\mathrm{i}(\Omega', z), \quad (10)$$

$$\frac{\partial}{\partial z}\hat{a}_\mathrm{i}(\Omega, z) = -g\int d\Omega' f(\Omega, \Omega', z)\hat{a}_\mathrm{s}(\Omega', z), \quad (11)$$

where

$$f(\Omega, \Omega', z) = \alpha_\mathrm{p}(\Omega - \Omega')e^{-i\Delta(\Omega,\Omega')z}, \quad (12)$$

$\alpha_\mathrm{p}(\Omega)$ is the amplitude of the pump classical field at the input of the crystal (since we assumed it does not evolve along z), $g = i\chi\mathcal{E}_\mathrm{p}\mathcal{E}_\mathrm{s}\mathcal{E}_\mathrm{i}/2\pi\hbar$ is a new coupling constant assumed to be real for simplicity, and the function $\Delta(\Omega, \Omega')$ is the phase mismatch between the signal, idler, and pump spectral components defined as

$$\Delta(\Omega, \Omega') = k_\mathrm{i}(\omega_\mathrm{i} + \Omega) - k_\mathrm{s}(\omega_\mathrm{s} + \Omega') - k_\mathrm{p}(\omega_\mathrm{p} + \Omega - \Omega'). \quad (13)$$

In the general case of plane waves that are noncollinear with the longitudinal axis z, the wave vector of each wave has a transverse component $\mathbf{q}_\mathrm{s}$, $\mathbf{q}_\mathrm{i}$, and $\mathbf{q}_\mathrm{p}$ for the signal, idler, and pump fields, respectively. In this case, $k_m(\omega)$ in Eqs. (1), (2), and (13) should be replaced by

$$k_{m,z}(\omega, \mathbf{q}_m) = \sqrt{k_m^2(\omega) - \mathbf{q}_m^2}. \quad (14)$$

The solution of Eqs. (10) and (11) can be obtained as a linear symplectic integral transformation for the field operators using the Magnus perturbative approach [61,62]. We will use the first-order Magnus approximation because, in this case, the modal quantities of our problem have analytic expressions. This approximation allows one to correctly describe conversion efficiency regimes around 80% [24,63], which are high enough for applications to quantum states. For regimes much closer to 100%, higher-order correction terms in the Magnus expansion should be considered. In this case, the modal approach still remains valid, but the expressions can now only be obtained by numerical methods. At the first order, we have

$$\begin{pmatrix}\hat{a}_\mathrm{s}(\Omega, l_c/2)\\ \hat{a}_\mathrm{i}(\Omega, l_c/2)\end{pmatrix} = e^{gl_c\mathbb{M}_1(\Omega)}\begin{pmatrix}\hat{a}_\mathrm{s}(\Omega', -l_c/2)\\ \hat{a}_\mathrm{i}(\Omega', -l_c/2)\end{pmatrix}, \quad (15)$$

where $\mathbb{M}_1(\Omega)$ is an integral transform operator whose action on any column vector $\mathbf{v}(\Omega) = [v_1(\Omega), v_2(\Omega)]^T$ is

$$\mathbb{M}_1(\Omega)\mathbf{v}(\Omega') = \int d\Omega'\begin{pmatrix}0 & K^*(\Omega', \Omega)\\ -K(\Omega, \Omega') & 0\end{pmatrix}\begin{pmatrix}v_1(\Omega')\\ v_2(\Omega')\end{pmatrix}, \quad (16)$$

l_c is the length of the nonlinear medium, and

$$K(\Omega, \Omega') = \frac{1}{l_c}\int_{-l_c/2}^{+l_c/2} dz\, f(\Omega, \Omega', z) = \alpha_\mathrm{p}(\Omega - \Omega')\,\mathrm{Sinc}\left[\Delta(\Omega, \Omega')\frac{l_c}{2}\right]. \quad (17)$$

Notice that the function $K(\Omega, \Omega')$ is not symmetric with respect to the exchange $\Omega \leftrightarrow \Omega'$ since the function $\Delta(\Omega, \Omega')$ is not either.

Then, by using the singular-value decomposition (SVD) of $K(\Omega, \Omega')$ that reads

$$K(\Omega, \Omega') = \sum_m \lambda_m\psi_m(\Omega)\phi_m^*(\Omega'), \quad (18)$$

the solution (15) can be put in the following form:

$$\begin{pmatrix}\hat{a}_\mathrm{s}(\Omega, l_c/2)\\ \hat{a}_\mathrm{i}(\Omega, l_c/2)\end{pmatrix} = \int d\Omega' B(\Omega, \Omega')\begin{pmatrix}\hat{a}_\mathrm{s}(\Omega', -l_c/2)\\ \hat{a}_\mathrm{i}(\Omega', -l_c/2)\end{pmatrix}, \quad (19)$$

where

$$B(\Omega, \Omega') = \begin{pmatrix}U_\mathrm{s}(\Omega, \Omega') & V_\mathrm{s}(\Omega, \Omega')\\ -V_\mathrm{i}(\Omega, \Omega') & U_\mathrm{i}(\Omega, \Omega')\end{pmatrix} \quad (20)$$

and

$$U_\mathrm{s}(\Omega, \Omega') = \sum_m \cos(gl_c\lambda_m)\phi_m(\Omega)\phi_m^*(\Omega'), \quad (21)$$

$$V_\mathrm{s}(\Omega, \Omega') = \sum_m \sin(gl_c\lambda_m)\phi_m(\Omega)\psi_m^*(\Omega'), \quad (22)$$

$$U_\mathrm{i}(\Omega, \Omega') = \sum_m \cos(gl_c\lambda_m)\psi_m(\Omega)\psi_m^*(\Omega'), \quad (23)$$

$$V_\mathrm{i}(\Omega, \Omega') = \sum_m \sin(gl_c\lambda_m)\psi_m(\Omega)\phi_m^*(\Omega'). \quad (24)$$

Hence the transformation induced by the time lens does not have a closed-form expression, but is given as an expansion in terms of the singular values λ_m and singular functions $\{\psi_m\}$ and $\{\phi_m\}$ of the idler and signal waves, respectively. Notice that if a signal waveform entering the crystal has the shape ϕ_m, then its output shape will remain unchanged, though part of its energy will be transmitted to the idler waveform having the shape ψ_m. The coincidence of input and output modal bases is a property of SFG in the first order of the Magnus expansion. In the general case, above 80% conversion efficiency, the output modes differ from the input ones for both interacting waves [16].

1. SFG configurations

The SFG process can be configured in different ways according to the chosen parameters for the pump and phase matching.

For what concerns the pump, a time lens is obtained when using a chirped Gaussian pulse. For this, a short Fourier-limited pulse of duration τ_p and spectral bandwidth Δ_p is dispersed through a medium of GDD, $D_\mathrm{p} = \beta_\mathrm{p}^{(2)} L_\mathrm{p}$, with L_p the length and $\beta_\mathrm{p}^{(2)}$ the group velocity dispersion of the medium. After the propagation, in the Fraunhofer dispersion limit, the pulse is stretched to a duration $\tau_\mathrm{p}' \gg \tau_\mathrm{p}$,

$$\tau_\mathrm{p}' = D_\mathrm{p} \Delta_\mathrm{p}. \tag{25}$$

In the Fourier domain, the chirped pulse is

$$\alpha_\mathrm{p}(\Omega) = A_\mathrm{p}\, e^{-\frac{1}{2}\Omega^2/\Delta_\mathrm{p}^2}\, e^{-\frac{i}{2}D_\mathrm{f}\Omega^2}, \tag{26}$$

where we define $D_\mathrm{f} = -D_\mathrm{p}$ as the *focal GDD* of the time lens.

For what concerns the phase matching, we can Taylor expand expression (13) up to first order in Ω and Ω',

$$\Delta(\Omega, \Omega')\frac{l_c}{2} \approx \Delta_0 \frac{l_c}{2} + (k_\mathrm{i}' - k_\mathrm{p}')\frac{l_c}{2}\Omega + (k_\mathrm{p}' - k_\mathrm{s}')\frac{l_c}{2}\Omega', \tag{27}$$

where $\Delta_0 = k_\mathrm{i}^0 - k_\mathrm{s}^0 - k_\mathrm{p}^0$ and k_m' are, respectively, the phase mismatch and the group velocity at the carrier frequency ω_m, for $m = \{s, i, p\}$. We restrict our treatment to processes that are perfectly phase matched at the central frequencies of the three waves so that $\Delta_0 = 0$. We can then distinguish three configurations that are qualitatively different:

(i) *Ideal*. In this case, not only is the phase matching perfect at carriers, but also for every Ω and Ω' so that $\Delta(\Omega, \Omega')l_c/2 = 0$. This condition would require one to simultaneously satisfy $(k_\mathrm{i}' - k_\mathrm{p}')l_c = 0$ and $(k_\mathrm{p}' - k_\mathrm{s}')l_c = 0$. The pump is assumed to be infinitely long.

(ii) *Perfect phase matching and finite aperture*. In this case, the aperture of the time lens is determined only by the (finite) pump duration τ_p' and it corresponds to the physical situation where the temporal walk-off between the pump and the signal and idler is much smaller than the inverse of the pump bandwidth, $\Delta_\mathrm{p}^{-1} = \tau_\mathrm{p}$. The conditions to be satisfied are now $|k_\mathrm{i}' - k_\mathrm{p}'|l_c \gg \tau_\mathrm{p}$ and $|k_\mathrm{p}' - k_\mathrm{s}'|l_c \gg \tau_\mathrm{p}$. From an experimental point of view, these conditions could be implemented by using symmetric group velocity matching $k_\mathrm{i}' - k_\mathrm{p}' = k_\mathrm{p}' - k_\mathrm{s}'$ (this condition is also known, in the case of parametric down-conversion, as "extended phase matching" [64]). Notice, however, that it is challenging to assure for the corresponding temporal walk-off to be larger than the reciprocal of the pump bandwidth. When these conditions are not respected, the temporal aperture is determined not only by the pump duration, but also by the spectral filtering induced by the phase matching. As a consequence, the time aperture would be smaller than that determined by the pump only. From a classical point of view, one could tune the other free parameter, the crystal length l_c, to be sufficiently small in order to satisfy those conditions. On the other hand, in the quantum regime, a small l_c would reduce the conversion efficiency that should be compensated by higher pump intensities. A different implementation could be via asymmetric group velocity matching, as discussed in [35,50], a configuration that is similar to that adopted for quantum pulse gates [23,29]. In the case where the pump and signal group velocities are matched $(k_\mathrm{p}' = k_\mathrm{s}')$, the spectral filtering of the phase matching does not limit the time lens aperture that is solely determined by the pump duration. However, the temporal walk-off between the idler and the pump introduces a spectral filtering that would be challenging to make negligible. As in the case of symmetric group velocity matching, one could, for example, use shorter crystals.

(iii) *Finite phase matching and finite aperture*. This is the most general case where no restrictions are required on the temporal walk-off and the pump duration. As discussed in [35,50], we consider the asymmetric group velocity dispersion matching $k_\mathrm{p}' = k_\mathrm{s}'$.

2. SVD in the Gaussian kernel approximation

In the configurations discussed above, the integral kernel $K(\Omega, \Omega')$ can be approximated by a double Gaussian. This allows one to obtain an analytic form for the singular values and the corresponding eigenvectors. When the group velocity of the pump is matched either to that of the signal or to that of the idler wave (asymmetric group velocity matching), the phase-matching function can be characterized by two bandwidths, Δ_h (along the horizontal direction) and Δ_v (along the vertical direction), so that (17) can be written as

$$\begin{aligned} K(\Omega, \Omega') \approx{}& A_\mathrm{p} e^{-\frac{1}{2}(\Omega-\Omega')^2/\Delta_\mathrm{p}^2} e^{-\frac{i}{2}D_\mathrm{f}(\Omega-\Omega')^2} \\ &\times e^{-\frac{1}{2}\Omega'^2/\Delta_\mathrm{h}^2} e^{-\frac{1}{2}\Omega^2/\Delta_v^2}, \end{aligned} \tag{28}$$

where the two characteristic bandwidths are given by the inverse of the temporal walk-off between the pump and signal waves $(\Delta_\mathrm{h}^{-1} = l_c|k_\mathrm{p}' - k_\mathrm{i}'|/2\sigma_0)$, or between the pump and the idler waves $(\Delta_\mathrm{v}^{-1} = l_c|k_\mathrm{p}' - k_\mathrm{s}'|/2\sigma_0)$, with $\sigma_0 = 1.61$ determined by approximating $\mathrm{Sinc}(x)$ with a Gaussian function $\exp(-x^2/2\sigma_0^2)$ having the same width at half maximum.

In this case, the SVD of $K(\Omega, \Omega')$ leads to the following analytic results (see Appendix A):

$$\lambda_m = A_\mathrm{p}\left[\frac{2\pi\,\widetilde{\Delta}_h\widetilde{\Delta}_v}{F_1 + F_2}\left(\frac{F_1 - F_2}{F_1 + F_2}\right)^m\right]^{1/2}, \tag{29}$$

$$\psi_m(\Omega) = \sqrt{\sigma_i}\, e^{-\frac{i}{2}D_\mathrm{f}(1-\widetilde{\Delta}_h^2/\Delta_\mathrm{p}^2)\Omega^2 + i\theta_m} u_m(\sigma_i\Omega), \tag{30}$$

$$\phi_m(\Omega) = \sqrt{\sigma_\mathrm{s}}\, e^{\frac{i}{2}D_\mathrm{f}(1-\widetilde{\Delta}_v^2/\Delta_\mathrm{p}^2)\Omega^2 - i\theta_m} u_m(\sigma_\mathrm{s}\Omega), \tag{31}$$

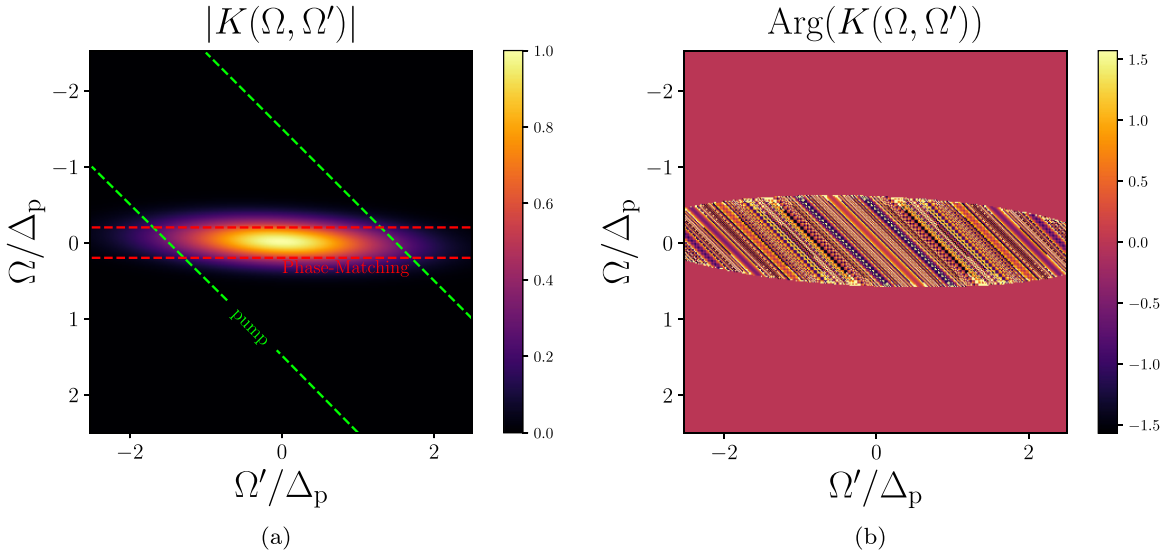

FIG. 2. (a) Modulus and (b) phase of $K(\Omega, \Omega')$ as described in Eq. (28). The parameters are $\Delta_\mathrm{p} = 10$ a.u., $\Delta_h = 10\Delta_\mathrm{p}$, $\Delta_v = 0.2\Delta_\mathrm{p}$, and $D_\mathrm{f} = 500\ \Delta_\mathrm{p}^{-2}$.

where $u_m(x) = (2^m m!\sqrt{\pi})^{-\frac{1}{2}} H_m(x) e^{-x^2/2}$ is the Gauss-Hermite function, $H_m(x)$ the Hermite polynomial, and

$$F_1 = \sqrt{1 + D_\mathrm{f}^2 \widetilde{\Delta}_h^2 \widetilde{\Delta}_v^2}, \tag{32}$$

$$F_2 = \sqrt{1 - \widetilde{\Delta}_h^2 \widetilde{\Delta}_v^2 / \Delta_\mathrm{p}^4}, \tag{33}$$

$$\sigma_\mathrm{i} = \sqrt{F_1 F_2}/\widetilde{\Delta}_v, \tag{34}$$

$$\sigma_\mathrm{s} = \sqrt{F_1 F_2}/\widetilde{\Delta}_\mathrm{h}, \tag{35}$$

with $1/\widetilde{\Delta}_h^2 = 1/\Delta_h^2 + 1/\Delta_\mathrm{p}^2$ and $1/\widetilde{\Delta}_v^2 = 1/\Delta_v^2 + 1/\Delta_\mathrm{p}^2$. Each mode has an order-dependent phase $\theta_m = (\theta_0 + m\theta)/2$, where θ_0 and θ are defined in Appendix A. The functions (30) and (31) belong to the family of chirped Gauss-Hermite functions, introduced first for studying propagation of optical pulses in fibers [65]. Some general properties of these functions have been established [66]. Some of their other properties, not met in the literature, are explored in Appendix B.

In the typical situation where $\Delta_v \ll \Delta_\mathrm{p} \ll \Delta_h$, the integral kernel $K(\Omega, \Omega')$ looks like the one depicted in Fig. 2, and $\widetilde{\Delta}_h \approx \Delta_\mathrm{p}$ and $\widetilde{\Delta}_v \approx \Delta_v$. In Figs. 3(a)–3(e), we trace the first 200 singular values, i.e., the first two signal (blue) and idler (green) eigenvectors for the indicated values of the parameters.

As a final remark, we observe that the multimode character of the time lens is grounded in the spectral correlations that come with the chirped pump phase profile [see Fig. 2(b)] and make $K(\Omega, \Omega')$ not separable. On the contrary, when the pump is not chirped ($D_\mathrm{f} = 0$), $K(\Omega, \Omega')$ is almost separable for $\Delta_v \ll \Delta_\mathrm{p} \ll \Delta_h$ and the process is single mode, as in the case of a quantum pulse gate [23,29].

III. MODAL APPROACH TO QUANTUM TEMPORAL IMAGING

In the case of perfect phase matching, the *imaging condition*, $1/D_\mathrm{in} + 1/D_\mathrm{out} = 1/D_\mathrm{f}$, and the Goodman-Tichenor approximation lead to a closed-form transformation for the scheme of Fig. 1(a) and to explicit expressions for the corresponding IRFs. We review these results in Appendix C.

For a nonideal phase matching [see configuration (iii) in Sec. II], it is not possible to analytically solve the propagation of field amplitudes through the time lens [Eqs. (10) and (11)] and a perturbative approach is required. In Sec. II B, we used the first order of the Magnus expansion that is suitable for high conversion efficiency regimes. This analysis leads to solutions (19) that are expressed in terms of the singular values and eigenfunctions of the kernel $K(\Omega, \Omega')$ [see Eq. (18)]. This explains the necessity of a modal approach to quantum temporal imaging.

The imaging transformation is obtained by applying, one after the other, the transformations given by Eq. (3) for the input dispersive propagation, Eq. (19) for the time lens, and Eq. (3) for the output dispersive propagation,

$$\hat{A}_\mathrm{i}^\mathrm{out}(\tau) = \int \frac{d\Omega}{2\pi}\, e^{-i\Omega\tau}\, \hat{a}_\mathrm{i}^\mathrm{out}(\Omega), \tag{36}$$

$$\hat{a}_\mathrm{i}^\mathrm{out}(\Omega) = \int d\Omega' \left[h_\mathrm{i}(\Omega, \Omega')\hat{a}_\mathrm{s}^\mathrm{in}(\Omega') + q_\mathrm{i}(\Omega, \Omega')\hat{a}_\mathrm{i}^\mathrm{in}(\Omega')\right], \tag{37}$$

where $h_\mathrm{i}(\Omega, \Omega')$ and $q_\mathrm{i}(\Omega, \Omega')$ are the two transfer functions given by

$$h_\mathrm{i}(\Omega, \Omega') = -\mathcal{G}_\mathrm{out}(\Omega) V_\mathrm{i}(\Omega, \Omega') \mathcal{G}_\mathrm{in}(\Omega'), \tag{38}$$

$$q_\mathrm{i}(\Omega, \Omega') = \mathcal{G}_\mathrm{out}(\Omega) U_\mathrm{i}(\Omega, \Omega'). \tag{39}$$

The classical IRF that allows one to quantify the system performances is then obtained by a Fourier transform of expression (38). We note that this is not a difficult task in the Gaussian kernel approximation since we deal with the Fourier transform of chirped Gauss-Hermite functions.

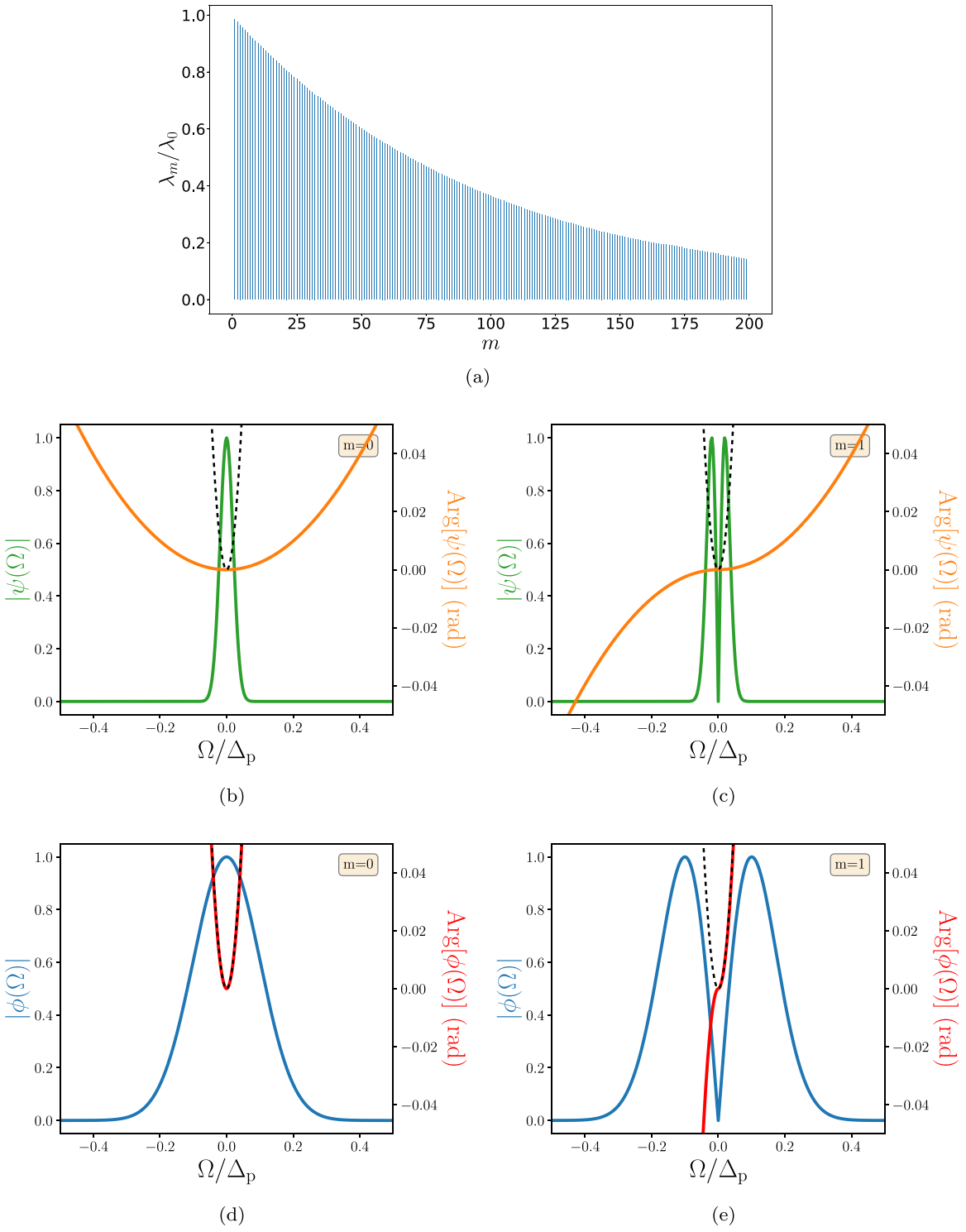

FIG. 3. For parameter choice $\Delta_\mathrm{p} = 10$ a.u., $\Delta_h = 10\Delta_\mathrm{p}$, $\Delta_v = 0.2\Delta_\mathrm{p}$, $D_\mathrm{f} = 500\ \Delta_\mathrm{p}^{-2}$: (a) singular values of $K(\Omega, \Omega')$, (b),(c) modulus and argument of first two output eigenvectors $m = 0$ and $m = 1$, (d),(e) modulus and argument of first two input eigenvectors $m = 0$ and $m = 1$. For comparison, we trace the quadratic phase $D_\mathrm{f}\Omega^2$ induced by the time lens (dashed-black lines).

Since the functions (38) and (39) satisfy the relation

$$\int d\Omega'' \left[h_\mathrm{i}(\Omega, \Omega'')h_\mathrm{i}^*(\Omega', \Omega'') + q_\mathrm{i}(\Omega, \Omega'')q_\mathrm{i}^*(\Omega', \Omega'')\right] = \delta(\Omega - \Omega'), \tag{40}$$

Eq. (36) is unitary and the field commutators are preserved at the output of the scheme,

$$\left[\hat{A}_\mathrm{i}^\mathrm{out}(\tau),\ \hat{A}_\mathrm{i}^{\mathrm{out}\,\dagger}(\tau')\right] = \delta(\tau - \tau'). \tag{41}$$

By using expressions (23) and (24), it is possible to write (38) and (39) in diagonal form,

$$h_{\rm i}(\Omega,\Omega') = \sum_m (-s_m)\xi_m(\Omega)\zeta_m^*(\Omega'), \tag{42}$$

$$q_{\rm i}(\Omega,\Omega') = \sum_m c_m \xi_m(\Omega)\psi_m^*(\Omega'), \tag{43}$$

where $s_m = \sin(gl_c\lambda_m)$, $c_m = \cos(gl_c\lambda_m)$, and

$$\xi_m(\Omega) = \mathcal{G}_{\rm out}(\Omega)\psi_m(\Omega), \tag{44}$$

$$\zeta_m(\Omega) = \mathcal{G}_{\rm in}^*(\Omega)\phi_m(\Omega). \tag{45}$$

Notice that the family of functions $\{\xi_m\}$ and $\{\zeta_m\}$ still forms two complete sets of orthonormal functions.

Even if it is not interesting from the point of view of quantum temporal imaging, for completeness, we also consider below the unitary transformation describing the output signal mode. The result is

$$\hat{A}_{\rm s}^{\rm out}(\tau) = \int \frac{d\Omega}{2\pi} e^{-i\Omega\tau}\hat{a}_{\rm s}^{\rm out}(\Omega), \tag{46}$$

$$\hat{a}_{\rm s}^{\rm out}(\Omega) = \int d\Omega' \left[h_{\rm s}(\Omega,\Omega')\hat{a}_{\rm i}^{\rm in}(\Omega') + q_{\rm s}(\Omega,\Omega')\hat{a}_{\rm s}^{\rm in}(\Omega')\right], \tag{47}$$

where, after using expressions (21) and (22),

$$h_{\rm s}(\Omega,\Omega') = \sum_m s_m\phi_m(\Omega)\psi_m^*(\Omega'), \tag{48}$$

$$q_{\rm s}(\Omega,\Omega') = \sum_m c_m\phi_m(\Omega)\zeta_m^*(\Omega'). \tag{49}$$

The ensemble of expressions (42), (43), (48), and (49) represents the decomposition of the full transformation associated to the imaging scheme in terms of singular values and eigenvectors.

Because of the completeness of $\{\zeta_m\}$, an input quantum object can be decomposed as

$$\hat{a}_{\rm s}^{\rm in}(\Omega) = \sum_m \hat{a}_{{\rm s},m}^{\rm in}\zeta_m(\Omega), \tag{50}$$

and hence the functions ζ_m can be regarded as degrees of freedom of the input object. Also, the input vacuum field can be decomposed as

$$\hat{a}_{\rm i}^{\rm in}(\Omega) = \sum_m \hat{a}_{{\rm i},m}^{\rm in}\psi_m(\Omega). \tag{51}$$

Then, because of the completeness of $\{\xi_m\}$, we can write the expansion

$$\hat{a}_{\rm i}^{\rm out}(\Omega) = \sum_m \left(-s_m\hat{a}_{{\rm s},m}^{\rm in} + c_m\hat{a}_{{\rm i},m}^{\rm in}\right)\xi_m(\Omega). \tag{52}$$

Typical experimental implementations, such as those discussed in Sec. II B, are far from the ideal situation since the signal-to-idler conversion efficiencies s_m fall off for increasing values of m. Therefore, in a general situation, the higher modal components of the signal object will be mixed with vacuum fluctuations at the output of the imaging scheme. As mentioned in Sec. II B, the present model is limited to a conversion efficiency of about 80%. However, had we extended its validity to the unit efficiency, it would not have predicted a noiseless imaging because the unit conversion efficiency would have not been possible for all modes. Since the singular values (29) of the process depend on the pump amplitude $A_{\rm p}$, it would have been possible to choose this value such that a particular s_m would have been equal to one, but this condition could not have been satisfied for all the rest of the eigenspectrum. For instance, let us consider, in the framework of the present model, a pump amplitude such that the fundamental modal component $m = 0$ presents 100% conversion efficiency in the firs-order Magnus perturbation theory ($s_0 = 1$ and $c_0 = 0$); this condition is reached when

$$gl_c\lambda_0 = \pi/2, \tag{53}$$

with λ_0 the most important singular value.

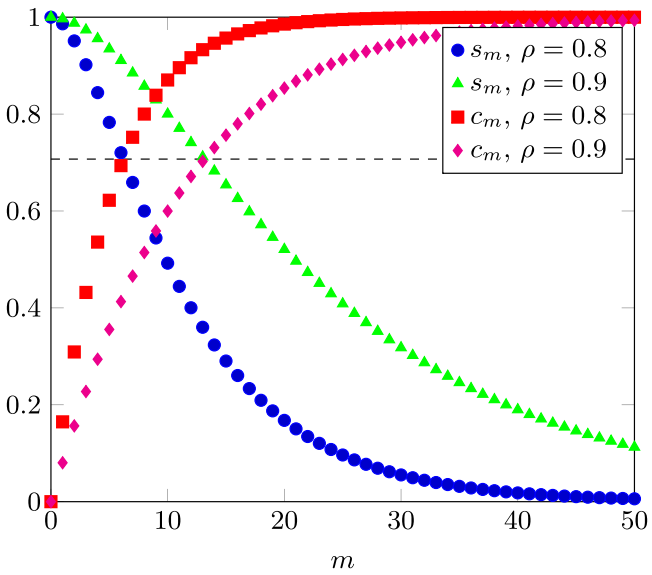

FIG. 4. Plot of $s_m = \sin(gl_c\lambda_m)$ (blue circles and green triangles) and $c_m = \cos(gl_c\lambda_m)$ (red squares and magenta diamonds) for $gl_c\lambda_0 = \pi/2$ and $\rho = \frac{F_1-F_2}{F_1+F_2} \in \{0.8, 0.9\}$.

In Fig. 4, we trace the values of coefficients s_m and c_m for an experimental situation corresponding to condition (53). From this figure, it is clear that while for the first eigenmode the situation is ideal, it rapidly gets worse for all the other modes: the higher the order m of the eigenmode, the higher the contribution c_m of the input vacuum fluctuations in the idler channel.

The modal analysis we have performed shows that the properties of the imaging transformation (37) are completely described by the set of coefficients s_m and c_m and by the family of eigenmodes, $\{\phi_m, \psi_m, \xi_m, \zeta_m\}$. This fact allows one to design optimal experimental configurations. Notice indeed that for a setup corresponding to larger values of the ratio

$$\rho = \frac{F_1 - F_2}{F_1 + F_2}, \tag{54}$$

the roll-off of the s_m coefficients is less important so that a larger number of modes is not corrupted by vacuum noise. One can appreciate this difference in Fig. 4, where the coefficients s_m for a $\rho = 0.9$ (green triangles) are compared to those corresponding to a smaller value $\rho = 0.8$ (blue dots). Since the parameters F_1 and F_2 depend on experimentally controllable parameters [see Eqs. (32) and (33)], highly

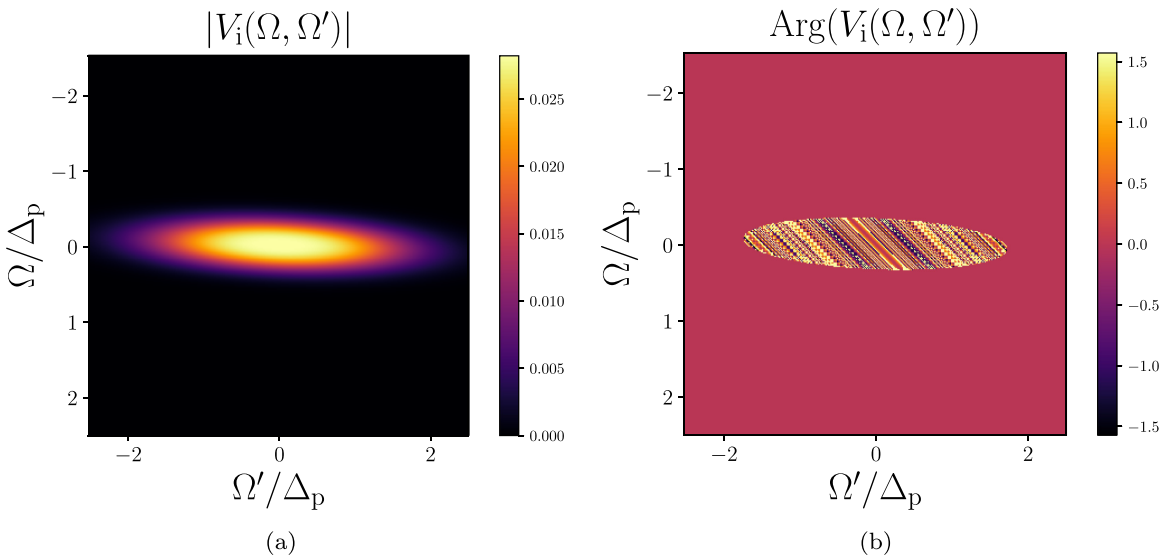

FIG. 5. (a) Modulus and (b) phase of $V_i(\Omega, \Omega')$ as described in Eq. (24). The parameters are $\Delta_p = 10$ a.u., $\Delta_h = 10\Delta_p$, $\Delta_v = 0.2\Delta_p$, and $D_f = 500\ \Delta_p^{-2}$.

multimode setups that are not dominated by quantum noise could be designed.

IV. QUANTIFICATION OF SYSTEM PERFORMANCES

While the performances of a temporal imaging scheme can be easily quantified in the case of perfect phase matching for any conversion efficiency regime, as soon as one wants to include the limitations induced by the finite phase matching, the quantification of performances becomes a difficult task. Despite the fact that the expressions (38) and (39) do not allow for an analytic evaluation of the transfer functions $h_i(\Omega, \Omega')$, $q_i(\Omega, \Omega')$, we show in this section that a quantitative assessment of the performances can be realized from the singular values and eigenvectors discussed in the previous section, thus showing the interest of the modal approach for temporal imaging.

As discussed by Bennett and Kolner in [35], a finite group velocity mismatch (GVM) between the three waves involved in the SFG process results in a spectral filtering that limits the bandwidth of the transmitted field amplitude and modifies the ideal impulse response $\tilde{h}(\tau)$. The resolution is now determined by the width of the effective IRF, $\tilde{h}'(\tau)$, that can be obtained, in two simplifying cases, as the convolution of the ideal IRF, $\tilde{h}(\tau)$, with the inverse Fourier transform of a spectral filtering function $\mathcal{F}(\tau)$: when the group velocity of the pump matches that of the signal, the GVM between pump and idler has the effect equivalent to a filter at the output. Hence, the total IRF is

$$\tilde{h}'(\tau) \propto \mathcal{F}_{\mathrm{out}}(\tau) * \tilde{h}(\tau), \tag{55}$$

where the asterisk denotes the convolution product. On the other side, when the group velocity of the pump matches that of the idler, the GVM between pump and signal has the effect equivalent to an input filter such that the total IRF is

$$\tilde{h}'(\tau) \propto \tilde{h}(\tau) * \mathcal{F}_{\mathrm{in}}(\tau/M), \tag{56}$$

with $M = -D_{\mathrm{out}}/D_{\mathrm{in}}$ the magnification factor of the imaging scheme.

In the low conversion efficiency regime, as the one considered by Bennett and Kolner, the filtering functions have an analytic expression, and therefore the bandwidth of their inverse Fourier transform can be obtained as $|k_p' - k_s'|l_c$ (respectively, $|k_p' - k_i'|l_c$). In the high conversion efficiency regimes, the time lens transformation (24) is significantly different from that in the low efficiency regime (17), and therefore the approach of [35] is less precise. This difference can be appreciated by comparing Figs. 2 and 5: at the first order of the Magnus expansion, the phase matching no longer has the profile of a double Gaussian as $K(\Omega, \Omega')$ and the spectral region where it is maximal is larger and flatter [compare Figs. 2(a) and 5(a)]. Also, this difference can be observed in Fig. 6 where the horizontal ($\Omega = 0$) and the vertical ($\Omega' = 0$) sections of $K(\Omega, \Omega')$ and $V_i(\Omega, \Omega')$ are compared. On the other side, the phase profile of $V_i(\Omega, \Omega')$ [see Fig. 5(b)] shows that the linear chirp induced by the pump is still present. This fact ensures that the scheme still works as a time lens in the high conversion efficiency regime.

The starting point of the modal approach consists in estimating the extension of the spectrum of the singular values $\{s_m\}$ by means of the Schmidt number S, which is defined as

$$S = \frac{\left(\sum_m s_m^2\right)^2}{\sum_m s_m^4}, \tag{57}$$

and characterizes the amount of degrees of freedom of the transformation (37). We assume below that this number is rounded to the nearest integer.

Spectral field of view. By the knowledge of the Schmidt number S, we can also get an estimate of the bandwidths of the horizontal (Δ_s) and vertical (Δ_s) sections of $|V_i(\Omega, \Omega')|$. Notice that these bandwidths also characterize the transfer function $h_i(\Omega, \Omega')$ by virtue of expression (38). These bandwidths can be approximately obtained as the variances of the eigenfunctions $\zeta_m(\Omega)$ and $\xi_m(\Omega)$ of order $m = S$. In the

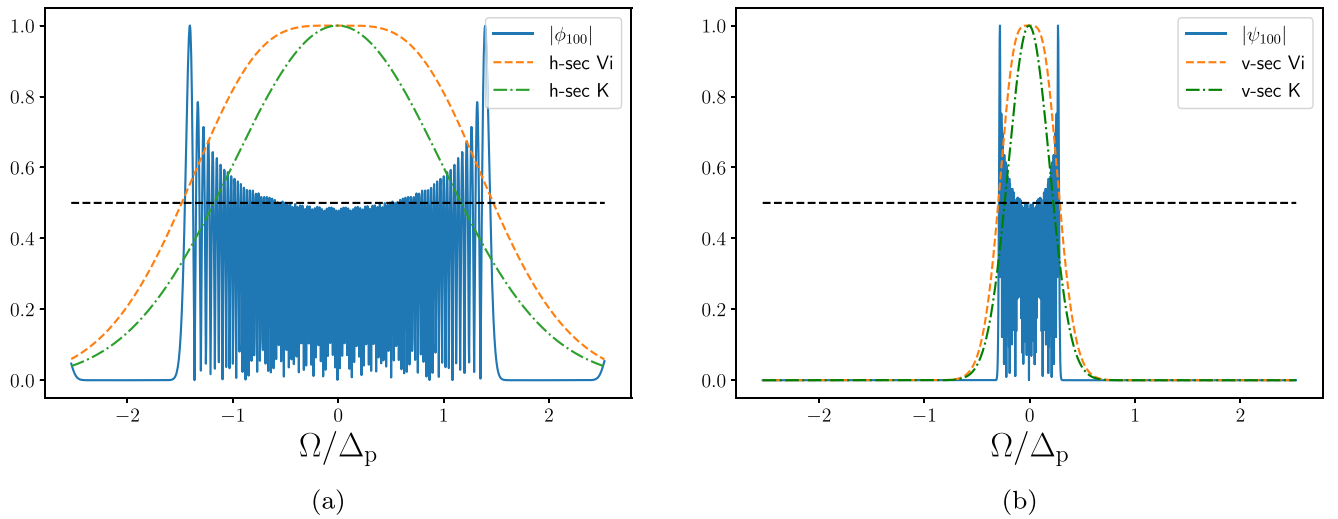

FIG. 6. For parameter choice $\Delta_p = 10$ a.u., $\Delta_h = 10\Delta_p$, $\Delta_v = 0.2\Delta_p$, $D_f = 500\ \Delta_p^{-2}$: (a) Comparison between the horizontal section ($\Omega = 0$) of $K(\Omega, \Omega')$ (green dash-dotted line) and that of $V_i(\Omega, \Omega')$ (yellow dashed line); the full width at half maximum of the horizontal section of $V_i(\Omega, \Omega')$ is close to the FWHM of the eigenmode $\phi_m(\Omega)$ with $m = S$ (in this case, $S = 100$). (b) Comparison between the vertical section ($\Omega' = 0$) of $K(\Omega, \Omega')$ (green dash-dotted line) and that of $V_i(\Omega, \Omega')$ (yellow dashed line); the full width at half maximum of the vertical section of $V_i(\Omega, \Omega')$ is close to the FWHM of the absolute value of eigenmode $|\psi_m(\Omega)|$ with $m = S$ (with $S = 100$).

Gaussian model, the eigenfunctions are chirped Gauss-Hermite functions; therefore, we get the analytic expressions (see Appendix B)

$$\Delta_s^2 = \left(S + \tfrac{1}{2}\right)\sigma_s^{-2}, \tag{58}$$

$$\Delta_i^2 = \left(S + \tfrac{1}{2}\right)\sigma_i^{-2}. \tag{59}$$

Temporal resolution. The Schmidt number and the eigenfunctions can be used for obtaining an analytic expression—in the case of the Gaussian approximation—of the resolution r of the imaging scheme. The resolution of an imaging scheme is the smallest detail that can be transferred; hence, by following [55], we can estimate r as the average distance, in the time domain, of the zeros of the Sth eigenfunction of the IRF: the smaller is r, the better is the resolution of the scheme. In the general case of nonideal phase matching, the transfer function $h_i(\Omega, \Omega')$ is characterized by the two families of eigenfunctions $\{\xi_m\}$ and $\{\zeta_m\}$ [see (42)]. In the time domain, the first family of eigenfunctions determines the characteristic time r_i of the system in the image plane, while the second family determines the characteristic time r_s in the object plane. Then the resolution of the system, at the image plane, is given by

$$r = \max\{|M| r_s, r_i\}, \tag{60}$$

where r_s and r_i are evaluated as the average distance of the zeros of the inverse Fourier transform of $\zeta_m(\Omega)$ and $\xi_m(\Omega)$ for $m = S$. This distance is given by the temporal width of the eigenfunction divided by the number of its semi-oscillations. By using the inverse Fourier transform of $\{\xi_m\}$ and $\{\zeta_m\}$, we find that the temporal widths (see Appendix B) for the eigenfunctions $m = S$ are

$$T_s = \sigma_s \sqrt{\left(S + \frac{1}{2}\right)\left(1 + \frac{(D_{in} - D_1)^2}{\sigma_s^4}\right)}, \tag{61}$$

$$T_i = \sigma_i \sqrt{\left(S + \frac{1}{2}\right)\left(1 + \frac{(D_{out} - D_2)^2}{\sigma_i^4}\right)}, \tag{62}$$

with $D_1 = D_f(1 - \widetilde{\Delta}_v^2/\Delta_p^2)$ and $D_2 = D_f(1 - \widetilde{\Delta}_h^2/\Delta_p^2)$. Notice that in T_s and T_i, the parameters σ_s, σ_i, and S depend on the details of the phase-matching profile of the SFG process, while the parameters D_{in} and D_{out} depend on the imaging scheme and are related to each other via the imaging condition [see Eq. (C14) in Appendix C].

Since the number of semi-oscillations for an Sth-order Gauss-Hermite function is given by S,

$$r_s = T_s/S, \tag{63}$$

$$r_i = T_i/S. \tag{64}$$

Temporal field of view (FOV). This figure of merit is defined as the temporal duration over which an object can be viewed. By following [35], let us assume that the input signal modes are made up of short classical features $f_{in}(\tau; \tau_0)$ centered at τ_0 and that, at the output, they are transformed as $f_{out}(\tau; \tau_0)$. Then the FOV is defined as the width of the energy profile $U(\tau_0)$ outgoing the system as a function of the input τ_0 of this feature,

$$U(\tau_0) \propto \int_{-\infty}^{+\infty} d\tau |f_{out}(\tau; \tau_0)|^2. \tag{65}$$

The estimation of this quantity in the case of a nonideal phase-matching profile requires a numerical calculation. However, the modal approach allows one to simplify expression (65). Indeed, by using (36) and the classical part of (52), we obtain

$$f_{out}(\tau; \tau_0) = \sum_{m=0}^{+\infty} (-s_m) f_{in,m}(\tau_0), \tag{66}$$

with

$$f_{\mathrm{in},m}(\tau_0) = \int_{-\infty}^{+\infty} d\tau\, \zeta_k^*(\tau) f_{\mathrm{in}}(\tau;\tau_0), \tag{67}$$

where $\zeta_k^*(\tau)$ is the Fourier transform of $\zeta_k^*(\Omega)$. As a consequence, one has

$$U(\tau_0) \propto \sum_{m=0}^{+\infty} s_m^2 |f_{\mathrm{in},m}(\tau_0)|^2. \tag{68}$$

Expression (68) can be considered a generalization of expression (28) in [35] for high conversion efficiency regimes and when the phase matching is nonideal. The FOV of the system can be estimated, then, by considering that the width of $U(\tau_0)$ is given by the width of the element $u_m(\tau_0)$ with $m = S$. As an example, consider an object pulse having infinitely small details such that $f_{\mathrm{in}}(\tau;\tau_0) \to \delta(\tau - \tau_0)$. In this case, $f_{\mathrm{in},m(\tau_0)} = \zeta_m^*(\tau_0)$ and the FOV is approximately given by the time duration of the input eigenvector corresponding to $m = S$; hence, FOV $\approx T_{\mathrm{s}}$.

As we discussed in [50], a time lens with a FOV designed for classical images is not necessarily adapted for the manipulation of a quantum image because while the degradation of its classical part might be negligible, at the same time it will be polluted by vacuum noise in a measure quantified by the c_m coefficients. The modal approach allows us to choose the level of acceptable added noise by simply choosing the maximum allowed, $c_{\max}$. From this choice, then, one can extract the order M such that $c_M \leqslant c_{\max}$. When $c_{\max} < 0.5$, then $M < S$. Hence, the quantum FOV corresponding to the chosen level of added noise can be defined such as the time duration of

$$\sum_{m=0}^{M} s_m^2 |f_{\mathrm{in},m}(\tau_0)|^2. \tag{69}$$

Time-bandwidth product. An important figure of merit in (temporal) imaging is the time-bandwidth product of the time lens. It corresponds to the number of (temporal) features that can be processed by a (time) lens and it is given by the ratio FOV$/r$ [35,36].

In order to improve the system performances, one has to increase the Schmidt number. This can be done by choosing the experimental parameters such that the ratio $\rho = (F_1 - F_2)/(F_1 + F_2)$ is as close as possible to one or, equivalently, $F_1 \gg F_2$. As an example, in Fig. 4, we compare two cases where the ratio ρ is changed from 0.8 to 0.9. This increment allows a doubling of S (from 6 to 13). Notice, however, that increasing the Schmidt number of the imaging scheme comes at a cost. Indeed, for any choice, since optimal conversion efficiency is obtained for $s_0 = 1$ or, equivalently, $g l_c \lambda_0 = \pi/2$, increasing the value of S means increasing the value of $g l_c A_{\mathrm{p}}$.

A. Ideal situation

The ideal situation [see configuration (i) in Sec. II] is reached when the phase matching is perfect over a very broad bandwidth $\Delta_h, \Delta_v \to +\infty$, when the pump bandwidth tends to infinity (faster than Δ_h and Δ_v), so that the pump pulse has a very large duration, $\tau_{\mathrm{p}}' = D_{\mathrm{f}} \Delta_{\mathrm{p}} \to +\infty$, and when the condition (53) for perfect conversion efficiency is satisfied. In this case, $F_1 \to D_{\mathrm{f}} \Delta_{\mathrm{v}} \Delta_{\mathrm{h}}$, $F_2 \to 1$, $\lambda_m = \lambda_0 = A_{\mathrm{p}} \sqrt{2\pi/D_{\mathrm{f}}}$, $s_m \approx 1$, and $c_m \approx 0$ for all m so that, from Eq. (52), no noise is introduced. The Schmidt number $S \to +\infty$ and, consequently, the bandwidths Δ_{s} and Δ_{i} are arbitrarily large and the parameters r_{s} and r_{i} are arbitrarily small.

Equation (42) in this case can be rewritten as

$$h_{\mathrm{i}}(\Omega, \Omega') = -\sum_m \xi_m(\Omega) \zeta_m^*(\Omega'). \tag{70}$$

On the other hand, we obtain, from Eqs. (18), (28), (44), and (45) in this limit,

$$\lambda_0 \sum_m \xi_m(\Omega) \zeta_m^*(\Omega') = A_{\mathrm{p}} \mathcal{G}_{\mathrm{out}}(\Omega) e^{-\frac{i}{2} D_{\mathrm{f}} (\Omega - \Omega')^2} \mathcal{G}_{\mathrm{in}}(\Omega'). \tag{71}$$

When the imaging condition (C14) is satisfied, we obtain, from Eqs. (70), (71), and (4),

$$h_{\mathrm{i}}(\Omega, \Omega') = -\sqrt{\frac{D_{\mathrm{f}}}{2\pi}} e^{-\frac{i}{2} M D_{\mathrm{f}} (\Omega - \Omega'/M)^2}, \tag{72}$$

where the magnification $M = -D_{\mathrm{out}}/D_{\mathrm{in}}$. In the temporal domain, this gives the well-known unitary transformation for perfect quantum temporal imaging [48],

$$\hat{A}_{\mathrm{out}}(\tau) = -\frac{1}{\sqrt{M}} e^{i \frac{\tau^2}{2 M D_{\mathrm{f}}}} \hat{A}_{\mathrm{in}}(\tau/M). \tag{73}$$

B. Perfect phase matching and finite aperture

In this section, we consider the case where the phase matching is almost perfect ($\Delta_h, \Delta_v \gg \Delta_{\mathrm{p}}$), but the imaging scheme presents a finite aperture induced by the pump pulse duration $\tau_{\mathrm{p}}' = D_{\mathrm{f}} \Delta_{\mathrm{p}}$ [see configuration (ii) in Sec. II B]. Notice that in this case, the traditional approach to temporal imaging (classical [33] and quantum [52]) gives analytic results as reviewed in Appendix C. The purpose of this section is, then, to test the modal approach developed in this paper by comparing its predictions to those obtained by the traditional approach. In Fig. 7, we show the modulus and argument of $K(\Omega, \Omega')$ as well as a comparison between the eigenspectrum of two nonideal configurations as those in Fig. 2 (blue solid and red dashed lines) and a configuration where the phase matching tends to be ideal (green dot-dashed line).

Here we have $\widetilde{\Delta}_h \approx \Delta_{\mathrm{p}}(1 - \Delta_{\mathrm{p}}^2/\Delta_h^2)$ and $\widetilde{\Delta}_v \approx \Delta_{\mathrm{p}}(1 - \Delta_{\mathrm{p}}^2/\Delta_v^2)$. Since, typically, the pump pulse is dispersed in the Fraunhofer limit ($D_{\mathrm{f}} \Delta_{\mathrm{p}}^2 \gg 1$), then $F_1 \approx D_{\mathrm{f}} \Delta_{\mathrm{p}}^2$ and $F_2 \approx \Delta_{\mathrm{p}}/\Delta_{hv}$, where

$$1/\Delta_{hv}^2 = 1/\Delta_h^2 + 1/\Delta_v^2. \tag{74}$$

Also, we have $\sigma_{\mathrm{i}} \approx \sqrt{D_{\mathrm{f}} \Delta_{\mathrm{p}}/\Delta_{hv}}$ and $\sigma_{\mathrm{s}} \approx \sqrt{D_{\mathrm{f}} \Delta_{\mathrm{p}}/\Delta_{hv}}$. The Schmidt number of the imaging scheme is large, $S \gg 1$, a consequence of the fact that the spectrum of s_m falls off very slowly. There is no explicit form for the expression of S in the general case; however, an underestimated value can be obtained in the low conversion regime (i.e., $g l_c \lambda_0 \ll \pi/2$) as $S \approx F_1/F_2$ or

$$S \approx \tau_{\mathrm{p}}' \Delta_{hv}. \tag{75}$$

By using this expression in (63) and (64), we find that $r_{\mathrm{s}} = (1 + 1/|M|) D_{\mathrm{f}}/\tau_{\mathrm{p}}'$ and $r_{\mathrm{i}} = (1 + |M|) D_{\mathrm{f}}/\tau_{\mathrm{p}}'$. Hence, in the

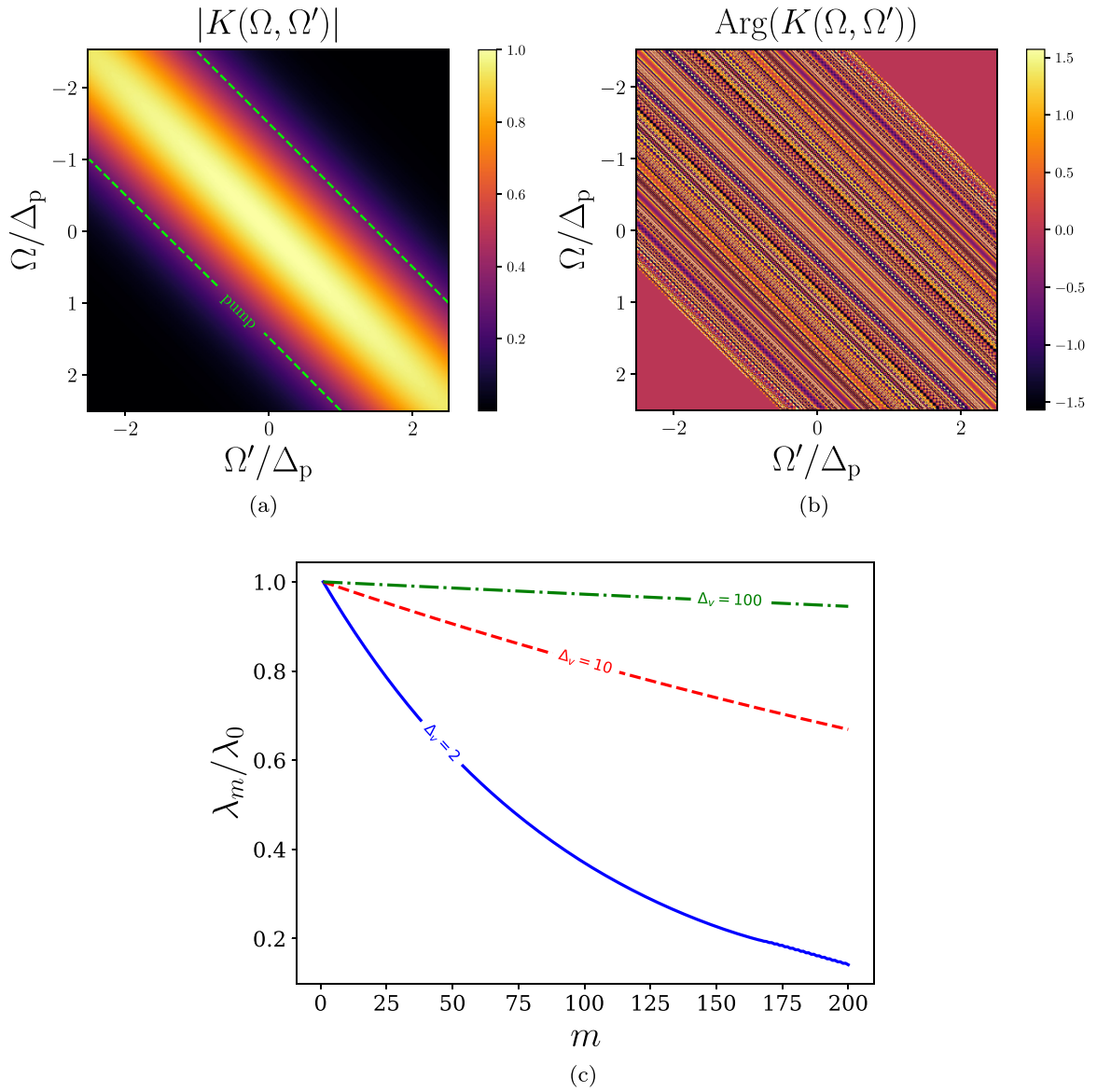

FIG. 7. (a) Modulus and (b) phase of $K(\Omega,\Omega')$ as described in Eq. (28) with parameters $\Delta_\mathrm{p} = 10$ a.u., $\Delta_h = 10\Delta_\mathrm{p}$, $\Delta_v = 10\Delta_\mathrm{p}$, and $D_\mathrm{f} = 500\Delta_\mathrm{p}^{-2}$. (c) Comparison between the eigenspectrum of three configurations tending to the perfect phase-matching case: solid blue for $\Delta_v = 0.2\Delta_\mathrm{p}$, dashed red for $\Delta_v = \Delta_\mathrm{p}$, and dot-dashed green for $\Delta_v = 10\Delta_\mathrm{p}$. Notice that the case $\Delta_v = 0.2\Delta_\mathrm{p}$ corresponds to the one depicted in Fig. 2.

limit of large magnification $|M| \gg 1$, the resolution r (60) is

$$r \approx |M| D_\mathrm{f}/\tau_\mathrm{p}', \tag{76}$$

and in the limit of large compression $|M| \ll 1$,

$$r \approx D_\mathrm{f}/\tau_\mathrm{p}', \tag{77}$$

which corresponds to the resolution obtained in [33] and [52].

Connection with the traditional approach is obtained by observing that in this limit [see (18)],

$$\sum_m \lambda_m \xi_m(\Omega)\zeta_m^*(\Omega') \approx \mathcal{G}_\mathrm{out}(\Omega)\alpha_\mathrm{p}(\Omega-\Omega')\mathcal{G}_\mathrm{in}(\Omega'). \tag{78}$$

As a result, the IRF is the Fourier transform of the pupil function of the scheme as described in [33,52] and detailed here in Appendix C.

It is interesting to observe that from the expressions of S, T_s, and T_i, the limit of $\Delta_h, \Delta_v \gg \Delta_\mathrm{p}$ gives arbitrary large values. However, their ratios (63) and (64) remain finite, as well as the system resolution.

C. Finite phase matching and finite aperture

This is the most general case [see configuration (iii) in Sec. II B], and we assume the typical situation where the group velocities of the pump and signal field are matched; in this case, hence, we have $\Delta_v \ll \Delta_\mathrm{p} \ll \Delta_h$. This situation corresponds to that depicted in Fig. 2. In this case, we have $\widetilde{\Delta}_v \approx \Delta_v$ and $\widetilde{\Delta}_h \approx \Delta_\mathrm{p}$. This implies that $F_1 \approx \tau_\mathrm{p}'\Delta_v$ and $F_2 \approx 1 - (\Delta_v/\sqrt{2}\Delta_\mathrm{p})^2$. Then the Schmidt number (in the low conversion regime) $S \approx \tau_\mathrm{p}'\Delta_v$ is smaller than that in the situation with perfect phase matching in Sec. IV B; we

assume below that $S \gg 1$. We also have $\sigma_s \approx \sqrt{D_f \Delta_v/\Delta_p}$ and $\sigma_i \approx \sqrt{D_f \Delta_p/\Delta_v}$.

For large magnification $|M| \gg 1$, we need to distinguish the cases $|M| \gg \Delta_p/\Delta_v$ and $|M| \ll \Delta_p/\Delta_v$. In the first case, the temporal durations of the eigenmodes $\zeta_S(\tau)$ and $\xi_S(\tau)$ are $T_s \approx \tau'_p \Delta_v/\Delta_p$ and $T_i \approx \tau'_p |M| \Delta_v/\Delta_p$, respectively. In this case, the resolution of the system, evaluated from (60), is

$$r \approx |M| r_s \approx r_i \approx |M| D_f/\tau'_p. \tag{79}$$

This result corresponds to Eq. (76) and to the resolution given by the traditional approach—the input resolution is given by the undispersed pump pulse width [35,52].

In the opposite case of $|M| \ll \Delta_p/\Delta_v$, we have $T_s \approx \tau'_p/|M|$ and $T_i \approx \tau'_p$. In this case, the resolution is

$$r \approx |M| r_s \approx r_i \approx \frac{D_f}{\tau'_p} \frac{\Delta_p}{\Delta_v}, \tag{80}$$

which differs from Eq. (79) by a factor $\Delta_p/|M|\Delta_v \gg 1$. This means that the resolution is greatly degraded by the effects of bandwidth filtering induced by the temporal walk-off between the pump and idler waves, as discussed in Ref. [35].

On the other side, for a system designed for a large compression $|M| \ll 1$, we have $T_s = \tau'_p/|M|$ and $T_i = \tau'_p$, and the resolution results in

$$r \approx \frac{D_f}{\tau'_p} \frac{\Delta_p}{\Delta_v}. \tag{81}$$

In this case, by comparison with (77), the resolution is always worse than that obtained for the perfect phase-matching case by a factor of Δ_p/Δ_v.

We see, thus, that the figures of merit calculated with the help of the modal approach coincide in the limiting cases with those obtained within the traditional approach based on the Fourier transform. In the intermediate cases, in particular, in a high conversion regime, these figures of merit can be evaluated by performing, analytically or numerically, the modal decomposition (18) and calculating the Schmidt number (57).

V. CONCLUSIONS

In this work, we developed the modal approach for a SFG-based quantum temporal imaging scheme in the high conversion efficiency regime and for the general case of nonperfect phase matching and finite temporal aperture. In general, this problem does not admit a closed-form expression for the IRF and for its Fourier transform, i.e., the transfer function. However, by using the modal approach, we showed that it is possible to express the transfer function in terms of its expansion on the singular values and eigenmodes of the problem. Then we showed how to obtain the relevant figures of merit of the imaging scheme and how to express them in terms of the modal decomposition. This allows one to assess the performances of the QTI scheme. We finally used these results for comparing the relevant figures of merit to those obtained in the regime of perfect phase matching and infinite aperture and of perfect phase matching and finite aperture. This comparison makes clear the necessity of a multimode operation for implementing a QTI scheme working in high conversion efficiency regimes and the physical parameters that need to be adjusted in order to improve its performances. Our results will allow, therefore, for better designs for noiseless manipulation of the spectrotemporal degrees of freedom of photonic nonclassical states.

ACKNOWLEDGMENTS

This work was supported by the network QuantERA of the European Union's Horizon 2020 research and innovation programme under project "Quantum information and communication with high-dimensional encoding" (QuICHE), the French part of which is funded by Agence Nationale de la Recherche via Grant No. ANR-19-QUAN-0001.

APPENDIX A: SINGULAR-VALUE DECOMPOSITION OF THE KERNEL

We can use the general formula for SVD of a complex double-Gaussian kernel [67],

$$e^{-\frac{1}{2}(\mu x^2+\nu y^2)+(\eta+i\xi)xy} = \sqrt{\frac{\pi\sigma_x\sigma_y}{v}} \sum_{k=0}^{\infty} p q^k u_k(\sigma_x x) u_k(\sigma_y y) e^{i\zeta\sigma_x^2 x^2 + i\zeta\sigma_y^2 y^2 + i(\theta_0 + k\theta)}, \tag{A1}$$

where μ, ν, η, and ξ are real numbers, satisfying the relations $\mu, \nu > 0$, $\sqrt{\mu\nu} > |\eta|$, necessary and sufficient for this kernel to be square integrable. On the right-hand side of Eq. (A1), $u_k(x)$ is the Gauss-Hermite function defined in Sec. II B, $\sigma_x = \sqrt{uv/v}$, $\sigma_y = \sqrt{uv/\mu}$, $\zeta = \eta\xi/(2uv)$, $p = \sqrt{2v/(u+v)}$, and $q = \sqrt{(u-v)/(u+v)}$, where $u = \sqrt{\mu\nu + \xi^2}$ and $v = \sqrt{\mu\nu - \eta^2}$. The phases are $\theta_0 = \arg(p_c)$ and $\theta = \arg(q_c)$, where

$$q_c = \frac{\eta + i\xi}{1 + w + i\eta\xi}, \tag{A2}$$

$$p_c = \sqrt{\frac{2w}{1 + w + i\eta\xi}}, \tag{A3}$$

and $w = \sqrt{(1+\xi^2)(1-\eta^2)}$.

Identifying $x = \Omega$, $y = \Omega'$, $\mu = \widetilde{\Delta}_v^{-2}$, $\nu = \widetilde{\Delta}_h^{-2}$, $\eta = \Delta_p^{-2}$, $\xi = D_f$, $u = F_1/\widetilde{\Delta}_v\widetilde{\Delta}_h$, $v = F_2/\widetilde{\Delta}_v\widetilde{\Delta}_h$, $\sigma_x = \sigma_i$, $\sigma_y = \sigma_s$, and $\zeta = D_f\widetilde{\Delta}_v^2\widetilde{\Delta}_h^2/2F_1F_2\Delta_p^2$, we obtain the decomposition of the kernel (28) into the singular functions (30) and (31).

APPENDIX B: SPECTRAL AND TEMPORAL WIDTHS OF CHIRPED GAUSS-HERMITE FUNCTIONS

We define a chirped Gauss-Hermite function as $u_n(x,\zeta) = u_k(x)\exp(i\zeta x^2)$, where $u_n(x)$ is the Gauss-Hermite function defined in Sec. II B and ζ is a real chirp parameter. Orthonormality and completeness of chirped Gauss-Hermite functions follow directly from the orthonormality and completeness of the Gauss-Hermite functions,

$$\int_{-\infty}^{+\infty} u_m(x,\zeta) u_n^*(x,\zeta) dx = \int_{-\infty}^{+\infty} u_m(x) u_n(x) dx = \delta_{mn}, \tag{B1}$$

$$\sum_{n=0}^{\infty} u_n(x,\zeta) u_n^*(x',\zeta) = \sum_{n=0}^{\infty} u_n(x) u_n(x') e^{i\zeta(x^2 - x'^2)} = \delta(x - x'). \tag{B2}$$

For every function of this basis, we treat $|u_n(x,\zeta)|^2$ as a probability density and define its moments

$$\langle x^k\rangle_{u_n} = \int_{-\infty}^{+\infty} x^k |u_n(x,\zeta)|^2 dx, \tag{B3}$$

and its standard deviation $\delta x_n = \sqrt{\langle x^2\rangle_{u_n} - \langle x\rangle_{u_n}^2}$. Using the symmetry property of Hermite polynomials $H_n(-x) = (-1)^n H_n(x)$, which also holds for the Gauss-Hermite functions, we arrive at a conclusion that $|u_n(x,\zeta)|^2$ is an even function of x and therefore all its odd moments are zero.

From the recurrence relations for the Hermite polynomials [68] $xH_n(x) = H_{n+1}(x)/2 + nH_{n-1}(x)$, we obtain the recurrence relations for chirped Gauss-Hermite functions,

$$xu_n(x,\zeta) = \frac{1}{\sqrt{2}}[\sqrt{n+1}u_{n+1}(x,\zeta) + \sqrt{n}u_{n-1}(x,\zeta)]. \tag{B4}$$

Substituting Eq. (B4) into Eq. (B3) and using the orthonormality of the chirped Gauss-Hermite functions, we obtain $\langle x^2\rangle_{u_n} = n + \frac{1}{2}$ and

$$\delta x_n = \sqrt{n+\tfrac{1}{2}}, \tag{B5}$$

which, of course, does not depend on the chirp parameter since the latter does not affect the modulus of a chirped Gauss-Hermite function.

Now we define the inverse Fourier transforms of chirped Gauss-Hermite functions,

$$\tilde{u}_n(y,\zeta) = \frac{1}{\sqrt{2\pi}}\int_{-\infty}^{+\infty} u_n(x,\zeta)e^{-ixy}dx. \tag{B6}$$

These functions also create a complete orthonormal set of functions, namely, the following relations hold:

$$\int_{-\infty}^{+\infty} \tilde{u}_m(y,\zeta)\tilde{u}_n^*(y,\zeta)dy = \delta_{mn}, \tag{B7}$$

$$\sum_{n=0}^{\infty} \tilde{u}_n(y,\zeta)\tilde{u}_n^*(y',\zeta) = \delta(y-y'), \tag{B8}$$

which can be proven by substituting Eq. (B6) and using Eqs. (B1) and (B2). Similarly to Eq. (B3), we define moments of Fourier-transformed functions,

$$\langle y^k\rangle_{\tilde{u}_n} = \int_{-\infty}^{+\infty} y^k |\tilde{u}_n(y,\zeta)|^2 dy, \tag{B9}$$

and their standard deviations, $\delta\tilde{y}_n = \sqrt{\langle y^2\rangle_{\tilde{u}_n} - \langle y\rangle_{\tilde{u}_n}^2}$.

From Eq. (B6), we find

$$\tilde{u}_n(-y,\zeta) = \frac{1}{\sqrt{2\pi}}\int_{-\infty}^{+\infty} u_n(-x,\zeta)e^{-ixy}dx = (-1)^n\tilde{u}_n(y,\zeta), \tag{B10}$$

and conclude that the odd moments of $|\tilde{u}_n(y,\zeta)|^2$ are zero. Recurrence relations for Fourier-transformed chirped Gauss-Hermite functions can be found by integration by parts, recurrence relations for Hermite polynomials written above, and their differential relations [68] $dH_n(x)/dx = 2nH_{n-1}(x)$:

$$\begin{aligned} y\tilde{u}_n(y,\zeta) &= \frac{i}{\sqrt{2\pi}}\int_{-\infty}^{+\infty}\left(\frac{d}{dx}e^{-ixy}\right)u_n(x,\zeta)dx \\ &= \frac{-i}{\sqrt{2\pi}}\int_{-\infty}^{+\infty}\frac{du_n(x,\zeta)}{dx}e^{-ixy}dx \\ &= \frac{i}{\sqrt{2}}[(1-2i\zeta)\sqrt{n+1}\tilde{u}_{n+1}(y,\zeta) \\ &\quad -(1+2i\zeta)\sqrt{n}\tilde{u}_{n-1}(y,\zeta)]. \end{aligned} \tag{B11}$$

Substituting Eq. (B11) into Eq. (B9) and using the orthonormality of the Fourier-transformed chirped Gauss-Hermite functions, we obtain $\langle y^2\rangle_{\tilde{u}_n} = (n+\frac{1}{2})(1+4\zeta^2)$ and

$$\delta\tilde{y}_n = \sqrt{(n+\tfrac{1}{2})(1+4\zeta^2)}. \tag{B12}$$

Thus, with growing chirp parameter, the width of the Fourier-transformed chirped Gauss-Hermite function is growing and its standard deviation grows almost linearly in the modulus of the chirp parameter for sufficiently high values of the latter.

APPENDIX C: STANDARD APPROACH IN THE PERFECT PHASE-MATCHING APPROXIMATION

Under the approximation of perfect phase matching, we get the results of [52] that we review in this section for comparison. Since, in this case,

$$f(\Omega,\Omega',z) \approx \alpha_{\rm p}(\Omega-\Omega'), \tag{C1}$$

the right-hand side of Eqs. (10) and (11) becomes convoluted and Eq. (15) reads

$$\begin{pmatrix}\hat{a}_{\rm s}(\Omega,l_c/2)\\ \hat{a}_{\rm i}(\Omega,l_c/2)\end{pmatrix} = e^{gl_cM(\Omega)*}\begin{pmatrix}\hat{a}_{\rm s}(\Omega,-l_c/2)\\ \hat{a}_{\rm i}(\Omega,-l_c/2)\end{pmatrix}, \tag{C2}$$

where $*$ denotes a convolution product and

$$M(\Omega) = \begin{pmatrix}0 & \alpha_{\rm p}^*(\Omega)\\ -\alpha_{\rm p}(\Omega) & 0\end{pmatrix}. \tag{C3}$$

Differently from the general case, solution (C2) is exact since all the terms of the Magnus expansion higher than the first order are all null, which is a well-known property of a perfectly phase-matched nonlinear process [61]. Then, by using inverse Fourier transform, the transformation (C2) becomes a standard matrix multiplication,

$$\begin{pmatrix}\hat{a}_{\rm s}(\tau,l_c/2)\\ \hat{a}_{\rm i}(\tau,l_c/2)\end{pmatrix} = B(\tau)\begin{pmatrix}\hat{a}_{\rm s}(\tau,-l_c/2)\\ \hat{a}_{\rm i}(\tau,-l_c/2)\end{pmatrix}, \tag{C4}$$

where

$$B(\tau) = \begin{pmatrix}c(\tau) & e^{-i\phi(\tau)}s(\tau)\\ -e^{i\phi(\tau)}s(\tau) & c(\tau)\end{pmatrix}, \tag{C5}$$

with $\phi(\tau) = \mathrm{Arg}[\tilde{\alpha}_{\rm p}(\tau)]$, $\tilde{\alpha}_{\rm p}(\tau)$ is the inverse Fourier transform of $\tilde{\alpha}_{\rm p}(\Omega)$,

$$\tilde{\alpha}_{\rm p}(\tau) \propto A_{\rm p}\, e^{-\tau^2/2\tau_{\rm p}'^2} e^{i\tau^2/2D_{\rm f}}, \tag{C6}$$

and

$$c(\tau) = \cos[gl_c|\tilde{\alpha}_p(\tau)|], \tag{C7}$$

$$s(\tau) = \sin[gl_c|\tilde{\alpha}_p(\tau)|]. \tag{C8}$$

In particular, the idler wave at the output ($z = l_c/2$) of the SFG process is given by

$$\hat{a}_i(\tau, l_c/2) = -e^{i\phi(\tau)}s(\tau)\hat{a}_s(\tau, -l_c/2) + c(\tau)\hat{a}_i(\tau, -l_c/2). \tag{C9}$$

Equation (C4) represents a unitary transformation of the photon annihilation operators from the input of the nonlinear crystal to its output, hence preserving the canonical commutation relations. This equation has the same form as the transformation induced by a beam splitter with the amplitude transmission coefficient $c(\tau)$ and the reflection coefficient $s(\tau)$ such that $c(\tau)^2 + s(\tau)^2 = 1$. The transmission coefficient controls the amount of the input waves that remains in the same mode and the reflection coefficient controls the amount of the input waves that is converted in the other mode. The phase factor $e^{i\phi(\tau)}$ in front of the input signal amplitude is determined by the phase of the pump wave. Therefore, a time lens transformation is obtained by choosing a quadratic time dependence in the pump phase, $\phi(\tau) = \tau^2/2D_f$. Notice that the second term on the right-hand side of (C9) is associated to vacuum fluctuations entering the nonlinear process through the input idler port of the time lens and mixing with the input state. These fluctuations are, of course, detrimental for the nonclassical input states and they need to be avoided. They can be suppressed when the conversion efficiency of the process $|s(\tau)|^2 = 1$. This situation can be reached when $gl_c|\alpha_p(\tau)| = \pi/2$. However, this condition cannot be satisfied for all τ because of a finite duration of the pump pulse. Typically, the pump pulse presents a maximum intensity at $\tau = 0$; then the conversion efficiency of the nonlinear process can be optimized such as

$$gl_c|\alpha_p(0)| = \pi/2, \tag{C10}$$

while for $\tau \neq 0$, the conversion efficiency will be smaller than one: as a consequence, the time lens presents a finite aperture of the imaging scheme.

The linear unitary transformation for the imaging scheme considered in Fig. 1(a) can be obtained by applying, one after the other, the transformation (3) for the input dispersive propagation with GDD D_{in}, then (C9) for the time lens, and, finally, (3) for the output dispersive propagation with GDD, D_{out}:

$$\hat{A}_i^{out}(\tau) = \int d\tau' \left[h_i(\tau, \tau')\hat{A}_s^{in}(\tau') + q_i(\tau, \tau')\hat{A}_i^{in}(\tau')\right], \tag{C11}$$

where

$$h_i(\tau, \tau') = -\int d\tau'' \, G_{out}(\tau - \tau'')s(\tau'')e^{i\tau''^2/2D_f} \times G_{in}(\tau'' - \tau'), \tag{C12}$$

$$q_i(\tau, \tau') = G_{out}(\tau - \tau')c(\tau') \tag{C13}$$

are the IRFs of the transformation. In [52], we showed that under the Goodman-Tichenor approximation and when the *imaging condition*

$$\frac{1}{D_{in}} + \frac{1}{D_{out}} = \frac{1}{D_f} \tag{C14}$$

is satisfied, then the IRFs become

$$h_i(\tau, \tau') = -i\sqrt{|M|}e^{\frac{-i\tau^2}{2|M|D_f}} \int \frac{d\Omega}{2\pi} e^{i\Omega(\tau - M\tau')}s(D_{out}\Omega), \tag{C15}$$

$$q_i(\tau, \tau') = i\sqrt{|M|}e^{\frac{-i\tau^2}{2|M|D_f}} \int \frac{d\Omega}{2\pi} e^{i\Omega(\tau - M\tau')}\tilde{c}(D_{out}\Omega), \tag{C16}$$

where $M = -D_{out}/D_{in}$ is the magnification factor of the imaging scheme and $\tilde{c}(\tau) = c(\tau)\exp(-i\tau^2/2D_f)$.

Notice that the response $h_i(\tau, \tau')$ corresponds to the classical IRF and is given, as in standard imaging, by the Fourier transform of the pupil function that in our case is the function $s(\tau)$. On the other side, the response $q_i(\tau, \tau')$ has no classical correspondence and is responsible for the vacuum fluctuations entering the scheme because of a finite pupil function.

When the pump pulse is infinitely long, and hence the temporal aperture of the lens is arbitrarily large, and the condition (C10) is satisfied, then $s(\tau) = 1$ and $c(\tau) = 0$. In this case, the response functions become ideal,

$$h_i(\tau, \tau') = -i\sqrt{|M|}e^{\frac{-i\tau^2}{2|M|D_f}}\delta(\tau - M\tau'), \tag{C17}$$

$$q_i(\tau, \tau') = 0, \tag{C18}$$

such that the transformation (C11)

$$\hat{A}_i^{out}(\tau) = -i\frac{e^{\frac{-i\tau^2}{2|M|D_f}}}{\sqrt{|M|}}\hat{A}_i^{in}(\tau/M) \tag{C19}$$

describes an ideal imaging scheme such as that considered in [44,48].

[1] B. Brecht, D. V. Reddy, C. Silberhorn, and M. G. Raymer, Phys. Rev. X **5**, 041017 (2015).

[2] M. Karpiński, A. O. C. Davis, F. Sośnicki, V. Thiel, and B. J. Smith, Adv. Quantum Technol. **4**, 2000150 (2021).

[3] P. C. Humphreys, B. J. Metcalf, J. B. Spring, M. Moore, X.-M. Jin, M. Barbieri, W. S. Kolthammer, and I. A. Walmsley, Phys. Rev. Lett. **111**, 150501 (2013).

[4] J. M. Lukens and P. Lougovski, Optica **4**, 8 (2017).

[5] V. S. Shchesnovich, Phys. Rev. A **89**, 022333 (2014).

[6] M. Pant and D. Englund, Phys. Rev. A **93**, 043803 (2016).

[7] J. Nunn, L. J. Wright, C. Söller, L. Zhang, I. A. Walmsley, and B. J. Smith, Opt. Express **21**, 15959 (2013).

[8] N. T. Islam, C. C. W. Lim, C. Cahall, J. Kim, and D. J. Gauthier, Sci. Adv. **3**, e1701491 (2017).

[9] P. Jian, O. Pinel, C. Fabre, B. Lamine, and N. Treps, Opt. Express **20**, 27133 (2012).
[10] J. M. Donohue, V. Ansari, J. Řeháček, Z. Hradil, B. Stoklasa, M. Paúr, L. L. Sánchez-Soto, and C. Silberhorn, Phys. Rev. Lett. **121**, 090501 (2018).
[11] M. Raymer and K. Srinivasan, Phys. Today **65**(11), 32 (2012).
[12] H. J. Kimble, Nature (London) **453**, 1023 (2008).
[13] S. Tanzilli, W. Tittel, M. Halder, O. Alibart, P. Baldi, N. Gisin, and H. Zbinden, Nature (London) **437**, 116 (2005).
[14] C. J. McKinstrie, J. D. Harvey, S. Radic, and M. G. Raymer, Opt. Express **13**, 9131 (2005).
[15] H. J. McGuinness, M. G. Raymer, C. J. McKinstrie, and S. Radic, Phys. Rev. Lett. **105**, 093604 (2010).
[16] M. G. Raymer, S. J. van Enk, C. J. McKinstrie, and H. J. McGuinness, Opt. Commun. **283**, 747 (2010).
[17] M. Karpiński, M. Jachura, L. J. Wright, and B. Smith, Nat. Photon. **11**, 53 (2017).
[18] F. Sośnicki and M. Karpiński, Opt. Express **26**, 31307 (2018).
[19] F. Sośnicki, M. Mikoajczyk, A. Golestani, and M. Karpiński, Appl. Phys. Lett. **116**, 234003 (2020).
[20] J. Lavoie, J. M. Donohue, L. G. Wright, A. Fedrizzi, and K. J. Resch, Nat. Photon. **7**, 363 (2013).
[21] M. Allgaier, V. Ansari, L. Sansoni, C. Eigner, V. Quiring, R. Ricken, G. Harder, B. Brecht, and C. Silberhorn, Nat. Commun. **8**, 14288 (2017).
[22] D. Kielpinski, J. F. Corney, and H. M. Wiseman, Phys. Rev. Lett. **106**, 130501 (2011).
[23] A. Eckstein, B. Brecht, and C. Silberhorn, Opt. Express **19**, 13770 (2011).
[24] D. V. Reddy, M. G. Raymer, C. J. McKinstrie, L. Mejling, and K. Rottwitt, Opt. Express **21**, 13840 (2013).
[25] B. Brecht, A. Eckstein, R. Ricken, V. Quiring, H. Suche, L. Sansoni, and C. Silberhorn, Phys. Rev. A **90**, 030302(R) (2014).
[26] P. Manurkar, N. Jain, M. Silver, Y.-P. Huang, C. Langrock, M. M. Fejer, P. Kumar, and G. Kanter, Optica **3**, 1300 (2016).
[27] D. V. Reddy and M. G. Raymer, Optica **5**, 423 (2018).
[28] V. Ansari, J. Donohue, B. Brecht, and C. Silberhorn, Optica **5**, 534 (2018).
[29] B. Brecht, A. Eckstein, A. Christ, H. Suche, and C. Silberhorn, New J. Phys. **13**, 065029 (2011).
[30] M. Allgaier, V. Ansari, J. M. Donohue, C. Eigner, V. Quiring, R. Ricken, and B. Brecht, and C. Silberhorn, Phys. Rev. A **101**, 043819 (2020).
[31] S. A. Akhmanov, A. P. Sukhorukov, and A. S. Chirkin, Zh. Eksp. Teor. Fiz. **55**, 1430 (1968) [Sov. Phys. JETP **28**, 748 (1969)].
[32] B. H. Kolner and M. Nazarathy, Opt. Lett. **14**, 630 (1989).
[33] B. H. Kolner, IEEE J. Quantum Electron. **30**, 1951 (1994).
[34] C. V. Bennett and B. H. Kolner, IEEE J. Quantum Electron. **36**, 430 (2000).
[35] C. V. Bennett and B. H. Kolner, IEEE J. Quantum Electron. **36**, 649 (2000).
[36] R. Salem, M. A. Foster, and A. L. Gaeta, Adv. Opt. Photon. **5**, 274 (2013).
[37] C. V. Bennett, R. P. Scott, and B. H. Kolner, Appl. Phys. Lett. **65**, 2513 (1994).
[38] C. V. Bennett and B. H. Kolner, Opt. Lett. **24**, 783 (1999).
[39] M. A. Foster, R. Salem, Y. Okawachi, A. C. Turner-Foster, M. Lipson, and A. L. Gaeta, Nat. Photon. **3**, 581 (2009).
[40] Y. Okawachi, R. Salem, M. A. Foster, A. C. Turner-Foster, M. Lipson, and A. L. Gaeta, Opt. Express **17**, 5691 (2009).
[41] O. Kuzucu, Y. Okawachi, R. Salem, M. A. Foster, A. C. Turner-Foster, M. Lipson, and A. L. Gaeta, Opt. Express **17**, 20605 (2009).
[42] M. A. Foster, R. Salem, D. F. Geraghty, A. C. Turner-Foster, M. Lipson, and A. L. Gaeta, Nature (London) **456**, 81 (2008).
[43] A. Tikan, S. Bielawski, C. Szwaj, S. Randoux, and P. Suret, Nat. Photon. **12**, 228 (2018).
[44] Y. Zhu, J. Kim, and D. J. Gauthier, Phys. Rev. A **87**, 043808 (2013).
[45] J. M. Donohue, M. D. Mazurek, and K. J. Resch, Phys. Rev. A **91**, 033809 (2015).
[46] S. Mittal, V. V. Orre, A. Restelli, R. Salem, E. A. Goldschmidt, and M. Hafezi, Phys. Rev. A **96**, 043807 (2017).
[47] J. Shi, G. Patera, D. B. Horoshko, and M. I. Kolobov, J. Opt. Soc. Am. B **37**, 3741 (2020).
[48] G. Patera and M. I. Kolobov, Opt. Lett. **40**, 1125 (2015).
[49] J. Shi, G. Patera, M. I. Kolobov, and S. Han, Opt. Lett. **42**, 3121 (2017).
[50] G. Patera, J. Shi, D. B. Horoshko, and M. I. Kolobov, J. Opt. **19**, 054001 (2017).
[51] J. Shi, G. Patera, Y. Gui, M. I. Kolobov, D. B. Horoshko, and S. Han, Chin. Opt. Lett. **16**, 092701 (2018).
[52] G. Patera, D. B. Horoshko, and M. I. Kolobov, Phys. Rev. A **98**, 053815 (2018).
[53] G. Patera, D. B. Horoshko, and M. I. Kolobov, Proc. SPIE **10771**, 1077107 (2018).
[54] C. Fabre and N. Treps, Rev. Mod. Phys. **92**, 035005 (2020).
[55] M. Bertero and E. R. Pike, Optica Acta: Intl. J. Opt. **29**, 727 (1982).
[56] M. I. Kolobov and C. Fabre, Phys. Rev. Lett. **85**, 3789 (2000).
[57] K. Piché, J. Leach, A. S. Johnson, J. Z. Salvail, M. I. Kolobov, and R. W. Boyd, Opt. Express **20**, 26424 (2012).
[58] Y. R. Shen, Phys. Rev. **155**, 921 (1967).
[59] D. B. Horoshko, Phys. Rev. A **105**, 013708 (2022).
[60] B. Huttner, S. Serulnik, and Y. Ben-Aryeh, Phys. Rev. A **42**, 5594 (1990).
[61] N. Quesada and J. E. Sipe, Phys. Rev. A **90**, 063840 (2014).
[62] T. Lipfert, D. B. Horoshko, G. Patera, and M. I. Kolobov, Phys. Rev. A **98**, 013815 (2018).
[63] A. Christ, B. Brecht, W. Mauerer, and C. Silberhorn, New J. Phys. **15**, 053038 (2013).
[64] V. Giovannetti, L. Maccone, J. H. Shapiro, and F. N. C. Wong, Phys. Rev. A **66**, 043813 (2002).
[65] P. Lazaridis, G. Debarge, and P. Gallion, Opt. Lett. **22**, 685 (1997).
[66] G. Cariolaro, M. Fregolent, A. Tonello, and C. De Angelis, Opt. Quantum Electron. **36**, 853 (2004).
[67] D. B. Horoshko, L. La Volpe, F. Arzani, N. Treps, C. Fabre, and M. I. Kolobov, Phys. Rev. A **100**, 013837 (2019).
[68] *Handbook of Mathematical Functions*, edited by M. Abramowitz and I. A. Stegun (Dover, New York, 1964).